



## Artificial thylakoid membrane assisted NiMn<sub>2</sub>O<sub>4</sub>@PoPDA hierarchical hollow nanospheres for photo-enzyme integrated catalysis

Jugong Shi<sup>a</sup>, Shiying Fan<sup>a</sup>, Xinyong Li<sup>a,\*</sup>, Penglei Wang<sup>a</sup>, Yan Mao<sup>a</sup>, Mufan Wang<sup>a</sup>, Guohua Chen<sup>b</sup>

<sup>a</sup> State Key Laboratory of Fine Chemicals, Key Laboratory of Industrial Ecology and Environmental Engineering (MOE), School of Environmental Science and Technology, Dalian University of Technology, Dalian 116024, PR China

<sup>b</sup> School of Energy and Environment, City University of Hong Kong, Kowloon Tong, Hong Kong, China



### ARTICLE INFO

#### Keywords:

Spinel  
Poly(o-phenylenediamine)  
Artificial thylakoid membrane  
Carbon fixation  
Photoenzymatic catalysis

### ABSTRACT

The selective functionalization of CO<sub>2</sub> is of profound significance concerning the global energy and environmental crisis. Herein, we cleverly designed and constructed a photoenzymatic system with a hierarchical hollow structure photo-enzyme integrated catalyst (nickel manganate -poly(o-phenylenediamine), NiMn<sub>2</sub>O<sub>4</sub>@PoPDA) by coating NiMn<sub>2</sub>O<sub>4</sub> with artificial thylakoid membrane (PoPDA) to mimic the characteristics of natural thylakoid membranes and combined formate dehydrogenase (FDH) to upgrade CO<sub>2</sub> to formic acid. The PoPDA membrane enhances the absorption of light energy and the efficiency of electron transfer, and improves the stability of the enzyme to avoid its deactivation. Most importantly, the favorable electronic coupling and band structure between NiMn<sub>2</sub>O<sub>4</sub> and PoPDA separate holes and electrons to afford a MV<sup>•+</sup> regeneration rate of 213.59 ± 4.91 mmol h<sup>-1</sup> g<sup>-1</sup> and a formic acid yield of 206 μmol. This work creates an efficient strategy using PoPDA as protector for enzyme stabilization to fabricate photobiocatalysts that realize highly efficient photoenzymatic catalysis.

### 1. Introduction

In synthetic chemistry, biocatalysts have become a rather competitive tool due to the exceptional chemoselectivity and stereospecificity [1,2], especially in the reduction of CO<sub>2</sub> to value-added compounds [3, 4]. The CO<sub>2</sub> reduction is often thermodynamically unfavorable [3,5], but among the various redox enzymes in biocatalysis, formate dehydrogenase (FDH) can overcome the thermodynamic barrier by stabilizing the intermediate through proton-coupled electron transfer reactions and converting CO<sub>2</sub> to formic acid [6,7]. Such process requires numerous methods for regeneration of NADH (β-nicotinamide adenine dinucleotide), which is used to provide the NADH stoichiometry depleted for sustained CO<sub>2</sub> reduction [8,9]. However, the process of regenerating reduced cofactors in nature involves complex electron transport chains and synthetic duplication of natural systems has shown to be particularly challenging. Therefore, it is crucial to add new pathways for carbon fixation.

Visible-light-mediated photocatalysis is a method to catalyze reactions under mild conditions. Inspired by natural photosynthesis, using

solar energy, a renewable energy source, for CO<sub>2</sub> conversion, providing new ideas for simultaneous CO<sub>2</sub> reduction and production of value-added compounds (methane, methanol, and formic acid) [10–12]. Currently, some photocatalysts used for CO<sub>2</sub> reduction such as inorganic semiconductor photocatalysts [13,14], covalent organic frameworks [15,16], carbon quantum dots [17], metal-organic frameworks [18,19], often suffer from poor product selectivity due to the multielectron reduction process and the competition of hydrogen evolution during CO<sub>2</sub> reduction [20,21]. Therefore, it is essential to develop robust photocatalytic systems that can efficiently and selectively convert CO<sub>2</sub> to specific value-added compounds.

Since the artificial photosynthesis system coupled with photocatalysis and biocatalysis has high similarity to the natural photosynthesis system, the integration of semiconductor photocatalyst with light-harvesting function and biocatalyst with CO<sub>2</sub>-processing capability will efficiently and selectively convert CO<sub>2</sub> into specific products. In principle, achieving synergy between photocatalysis and biocatalysis requires NAD<sup>+</sup>/NADH as redox mediators. But employing NAD<sup>+</sup>/NADH for CO<sub>2</sub> reduction to formate will have the following three disadvantages: (1) the

\* Corresponding author.

E-mail address: [xli@dlut.edu.cn](mailto:xli@dlut.edu.cn) (X. Li).

equilibrium constant of the reaction is large reaching  $10^7$  [22], which makes the generated formic acid rapidly oxidized to  $\text{CO}_2$ , which reduces the net yield of formate; (2) high concentration of NADH will inhibit the function of FDH [23]; and (3) the reduction product NADH is prone to isomerization and dimerization [24]. Therefore, the process that occurs in nature is reversed by selecting other redox cofactors that have good binding properties with FDH. It was found that the artificial cofactor methyl viologen ( $\text{MV}^{2+}/\text{MV}^{\bullet+}$ ) can inhibit the oxidation of formate to  $\text{CO}_2$  by FDH [25,26].  $\text{MV}^{2+}$  can act as both an electron mediator to transfer electrons and a redox mediator to achieve the connectivity between photocatalysis and biocatalysis, achieving the effect of “two birds with one stone”. Additionally, the effective regeneration of artificial cofactors relies on the exquisite design and construction of photocatalysts with appropriate structures.

Hollow nanostructures have unique advantages over their solid nanostructures [27]. The inner cavity facilitates the separation of photogenerated electron-hole pairs by reducing the bulk-to-surface diffusion distance and provides large surface area, which promotes the adsorption of reactants and surface-dependent chemical reactions on both the outer and inner shells. Although, enzymes have high activity and selectivity, it suffers from poor stability. Therefore, it is very important to avoid enzyme inactivation by reactive oxygen species (ROS) by constructing a “wall” between enzymes and photocatalysts [28]. In nature, thylakoid membrane is a multifunctional membrane structure with a distribution of pigments and proteins related to photosynthetic light reactions to increase the absorption of light energy and efficient electron transfer (Fig. 1) [29,30]. Ideally, natural thylakoid membranes were modeled with high performance organic polymers poly(o-phenylenediamine) (PoPDA). PoPDA has been polymerized from o-phenylenediamine (oPD) monomers, and these polymers can improve electrical conductivity, cycle utilization and electron transfer efficiency [31]. Moreover, carbonaceous materials compounded with semiconductors have excellent light capture and anti-photocorrosion performances. Meanwhile, the electron-accepting/-transfer properties of the introduced carbon species can provide a better path to guide the transport of charge carriers, extending their lifetime and ultimately improving the photocatalytic performance. Importantly, the doping of nitrogen is believed to further improve the electronic and chemical features of carbon-based materials, thus enhancing the photochemical performances [32].

Taking together above, we focused on the construction of an artificial thylakoid membrane to achieve the compatible coexistence between FDH and photocatalyst (Fig. S1), consequently maintaining the original high activity of the enzyme. Here, we designed and synthesised hierarchical hollow nanostructures ( $\text{NiMn}_2\text{O}_4@\text{PoPDA}$ , denoted as NMO@PoPDA) with artificial thylakoid membranes constructed from PoPDA and nickel manganate nanospheres ( $\text{NiMn}_2\text{O}_4$ , denoted as NMO). Using NMO@PoPDA as photocatalyst and employing  $\text{MV}^{2+}$  as artificial

cofactors to couple with formate dehydrogenase from *Candida boidinii* (CbFDH) for the reduction of  $\text{CO}_2$  to formic acid under visible light (Fig. S2). Taking advantage of good solar energy capture ability of PoPDA membrane, efficient electron transport, excellent biocompatibility, strong electron coupling in NMO@PoPDA catalyst and good band structure, this photo-enzyme coupled system could efficiently realize  $\text{CO}_2$  reduction with a formate yield of 206  $\mu\text{mol}$ .

## 2. Results and discussion

### 2.1. Preparation and characterization of hierarchical hollow NMO@PoPDA nanospheres with artificial thylakoid membrane

The preparation strategy for hierarchical hollow NMO@PoPDA nanospheres with artificial thylakoid membrane is shown in Fig. 2a. Briefly, NMO hollow nanospheres were prepared by solvothermal method to support in-situ polymerization and growth of o-phenylenediamine on the outer surface to form a poly(o-phenylenediamine) coating. A tightly bonded oligomer coating is formed on the NMO surface by photoinitiated in-situ oxidative polymerization, which is used as an artificial thylakoid membrane to separate photocatalytic oxidation and enzymatic  $\text{CO}_2$  reduction.

Scanning electron microscopy (SEM) and transmission electron microscopy (TEM) were used to study the morphology of the as-prepared NMO and hierarchical hollow NMO@PoPDA nanospheres. As shown in Fig. 2b, the NMO nanosphere surface is relatively smooth, and the NMO@PoPDA is wrinkled (Fig. 2c), indicating that NMO is successfully encapsulated by PoPDA. Hollow NMO nanospheres were successfully prepared with diameters of 200–400 nm (Fig. 2d). Poly(o-phenylenediamine) oligomers were found to grow evenly and tightly on the surface of NMO nanospheres, constructing the hierarchical hollow NMO@PoPDA nanospheres structure with artificial thylakoid membrane (Fig. 2e). Further, high-angle annular dark field (HADDF) and elemental mappings images (Fig. 2f-j) exhibited the existence of Ni, Mn, C, and N elements, which were evenly distributed in the structure.

Powder X-ray diffraction (XRD) and Fourier transform infrared spectroscopy (FTIR) were performed to determine the chemical structure of NMO@PoPDA-x, NMO\* (solid nanospheres) and NMO\*@PoPDA (Fig. S3 and Fig. S4). The diffraction peaks of samples correspond to NMO (JCPDS No. 01-1110) and PoPDA (CCDC No. 158272) [33,34]. For the NMO nanospheres, several peaks centered at 35.8, 43.6, 57.5, 63.3 were observed, corresponding to the (311), (400), (511) and (440) crystal planes of NMO, respectively, indicating that the prepared materials exhibit NMO crystalline properties. In the NMO@PoPDA-x nanospheres, the peak intensities of NMO revealed significant decrease with the increasing content of PoPDA, suggesting that the excess PoPDA coverage had a shield function on the interior NMO spheres. The FTIR spectrum is shown in Fig. S4. The peak positioned at  $605\text{ cm}^{-1}$  related to the Ni-O stretching vibration of the tetrahedral site [35]. The peak at  $3150\text{ cm}^{-1}$ – $3450\text{ cm}^{-1}$  represented the stretching vibration of  $-\text{NH}-$  /  $-\text{NH}_2$ . The characteristic peaks located at  $1100\text{ cm}^{-1}$ – $1640\text{ cm}^{-1}$  can be attributed to the skeletal vibrations of aromatic CN heterocycles [31]. The absorption peaks and changes of FTIR prove that the polymerization reaction has occurred. The above results reveal that NMO nanospheres were successfully coated with PoPDA. The elemental composition and surface chemical states of NMO@PoPDA-2 were analyzed by x-ray photoelectron spectroscopy (XPS). The high-resolution XPS spectra of Ni 2p, Mn 2p, C 1s, and N 1s are shown in Fig. 3a-d. For the Ni species of NMO, the high-resolution Ni 2p spectrum is well fitted considering the two spin-orbit double characteristic of  $\text{Ni}^{2+}$  and  $\text{Ni}^{3+}$  with binding energy at 854.5 eV, 872.2 eV, and 856 eV, 873.8 eV respectively. In addition, the peaks at around 861.4 and 879.9 eV are indexed to the shake-up satellites of nickel (Fig. 3a) [36,37]. In the Mn 2p spectrum (Fig. 3b), three kinds of Mn species are detected. The binding energy at 638.7 and 652.4 eV are ascribed to  $\text{Mn}^{2+}$ , 642.0 and 653.6 eV are attributed to  $\text{Mn}^{3+}$ , and

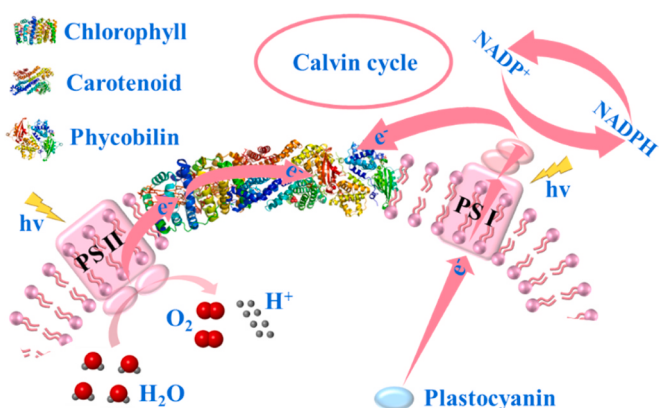
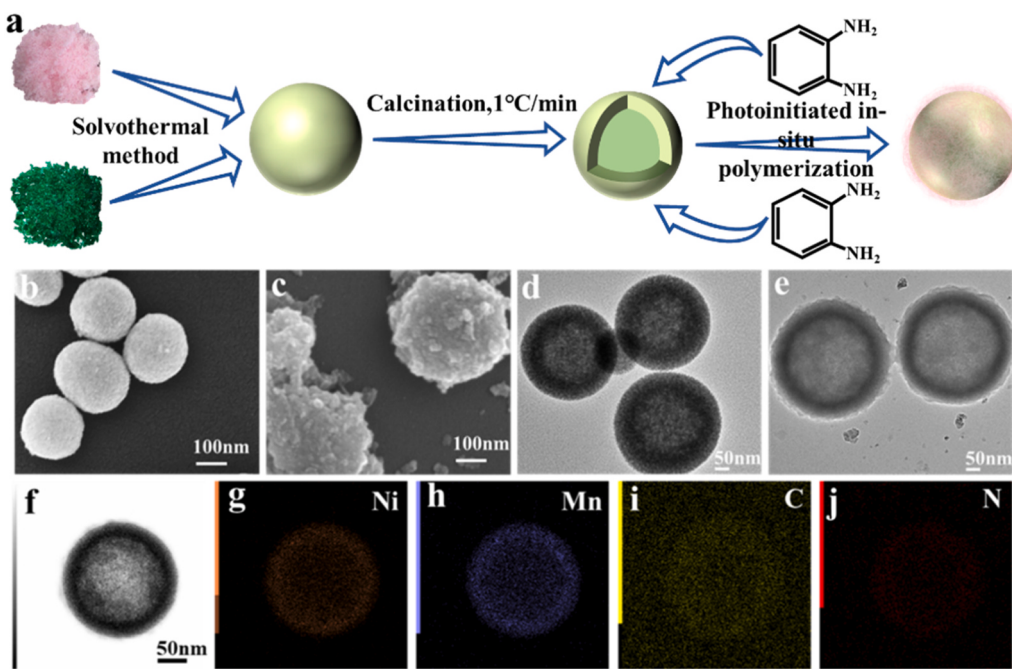


Fig. 1. Membrane structure of thylakoid in nature.

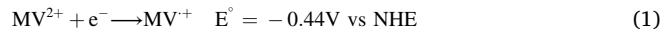


**Fig. 2.** (a) Schematic illustration for fabricating hierarchical hollow NMO@PoPDA nanospheres. SEM images of (b) NMO and (c) NMO@PoPDA-2. TEM images of (d) NMO and (e) NMO@PoPDA-2. (f) HAADF image, and (g-j) EDS mappings of NMO@PoPDA-2.

another pair of peaks at 644.2 and 655 eV are assigned to Mn<sup>4+</sup> [33]. For pure PoPDA, its N 1 s spectrum is deconvoluted into two separate peaks located at binding energies of 398.5 and 400.1 eV, corresponding to the –NH– / –NH<sub>2</sub> and =N – (Fig. 3c) [34,36]. The characteristic peaks at 284.8, 286.6 and 288.7 eV can correspond to C=C, C–N, and N = C–N (Fig. 3d) [31,38]. Moreover, compared with NMO and PoPDA, significant peak shifts were observed in the XPS spectrum of Ni 2p, Mn 2p, N 1 s and C 1 s of NMO@PoPDA-2 nanospheres, demonstrating the strong interaction between NiMn<sub>2</sub>O<sub>4</sub> and PoPDA. Thus, the tight growth of PoPDA on NMO nanospheres facilitates the formation of close interfacial connections, which is conducive to charge separation and transfer of NMO@PoPDA-2.

UV-vis diffuse reflectance (DR) measurement was then employed to investigate the optical properties of NMO and PoPDA catalyst (Fig. S5). Both NMO and NMO@PoPDA-x nanospheres exhibit excellent visible-light response. NMO@PoPDA-x enables enhanced optical absorption of NMO, owing to the light muti-reflection and scatterings inside hollow structure and narrow bandgap (1.8 eV) of PoPDA. From the Kubelka-Munk function, it can be concluded that the optical band gaps of NMO and PoPDA are 2.03 and 1.8 eV, respectively (Fig. 4a). The valence band (VB) XPS spectroscopy was employed to measure the VB edge potential of catalyst, the valence-band maximum of NMO and PoPDA were determined to be 1.11 and 1.26 eV, respectively (Fig. 4b). The conduction band (CB) potential of NMO and PoPDA were deduced to be –0.92 and –0.54 eV, respectively, proving that both samples possess thermodynamic driving forces for ROS generation [39]. Based on the above analysis, the relative energy levels of NMO and PoPDA were schematically depicted in Fig. 4c. According to Eq. (1), both NMO and PoPDA can regenerate MV<sup>•+</sup> due to the lower redox potential of the MV<sup>2+</sup>/MV<sup>•+</sup> couple than the CB of the samples [22,40]. The corresponding cyclic voltammogram (CV) curves (Fig. S6) demonstrate that NMO@PoPDA-2 has a wider closed curve and a redox peak at –1.172 V (vs Ag/AgCl, pH=7), directly confirming that the redox reaction occurred when electrons were transferred from NMO to PoPDA. Then the reduction potential was converted to –0.552 V (vs NHE, pH=0), implying that the electrons generated on NMO@PoPDA-2 could be efficiently transferred to the artificial cofactor MV<sup>2+</sup>. However, compared to NMO@PoPDA-2, no redox peak was observed in the range

of –0.4 V to –1.36 V for CV, suggesting the redox inactive nature of NMO in such potential window.



Here, the PoPDA membrane was used as a conductive layer, which would transfer electrons through the CB [41]. Thus, the photogenerated electrons on the NNO were first transported to the PoPDA membrane and then captured by MV<sup>2+</sup> to regenerate MV<sup>•+</sup>. Also, to compartmentalize photocatalytic oxidation and enzymatic reduction, the PoPDA membrane should block the permeation of CbFDH but still support TEOA entry. The pore diameter on the membrane was determined to be 2.7 nm by the N<sub>2</sub> adsorption-desorption isotherm curve (Fig. 4d), which is smaller than the CbFDH protein size determined by the Pymol visualization software.

## 2.2. Photocatalytic activities of hierarchical hollow NMO@PoPDA-x nanospheres catalysts

The methyl viologen cation was regenerated using NMO@PoPDA-x and NMO<sup>\*</sup>@PoPDA photocatalysts and the photocatalyst activity was expressed in terms of MV<sup>•+</sup> concentration. The photocatalytic MV<sup>•+</sup> regeneration was performed under the following conditions by using TEOA as the electron donor, a 400 W xenon lamp (filter out ultraviolet light), anaerobic and MV<sup>2+</sup> as the electron mediator. The concentration of MV<sup>•+</sup> was determined using molar extinction coefficient at 605 nm ( $\varepsilon = 1.3 \times 10^4 \text{ M}^{-1} \text{ cm}^{-1}$ ) [22]. To exclude the effect of light, we first used full-spectrum ( $\lambda \geq 300 \text{ nm}$ ) irradiation for the solution containing methyl viologen in the absence of catalyst and under anaerobic conditions. UV-visible spectroscopy studies show no decrease in the concentration of MV<sup>2+</sup> or the appearance of MV<sup>•+</sup> absorption peaks (Fig. S7). As shown in Fig. 4e, the NMO@PoPDA-2 performs the best photocatalytic activity (regeneration concentration  $213.59 \pm 4.91 \text{ mmol h}^{-1} \text{ g}^{-1}$ ), which was 2.3- and 2.8-fold of NMO<sup>\*</sup>@PoPDA ( $92.25 \pm 2.06 \text{ mmol h}^{-1} \text{ g}^{-1}$ ) and PoPDA ( $77.43 \text{ mmol h}^{-1} \text{ g}^{-1}$ ), respectively (Fig. S8). Intriguingly, the as-prepared NMO@PoPDA-2 catalyst shows satisfactory high activity in visible light-driven CO<sub>2</sub> reduction to formic acid production in the previously reported photo-enzyme coupled system. (Table S1). Additionally, the

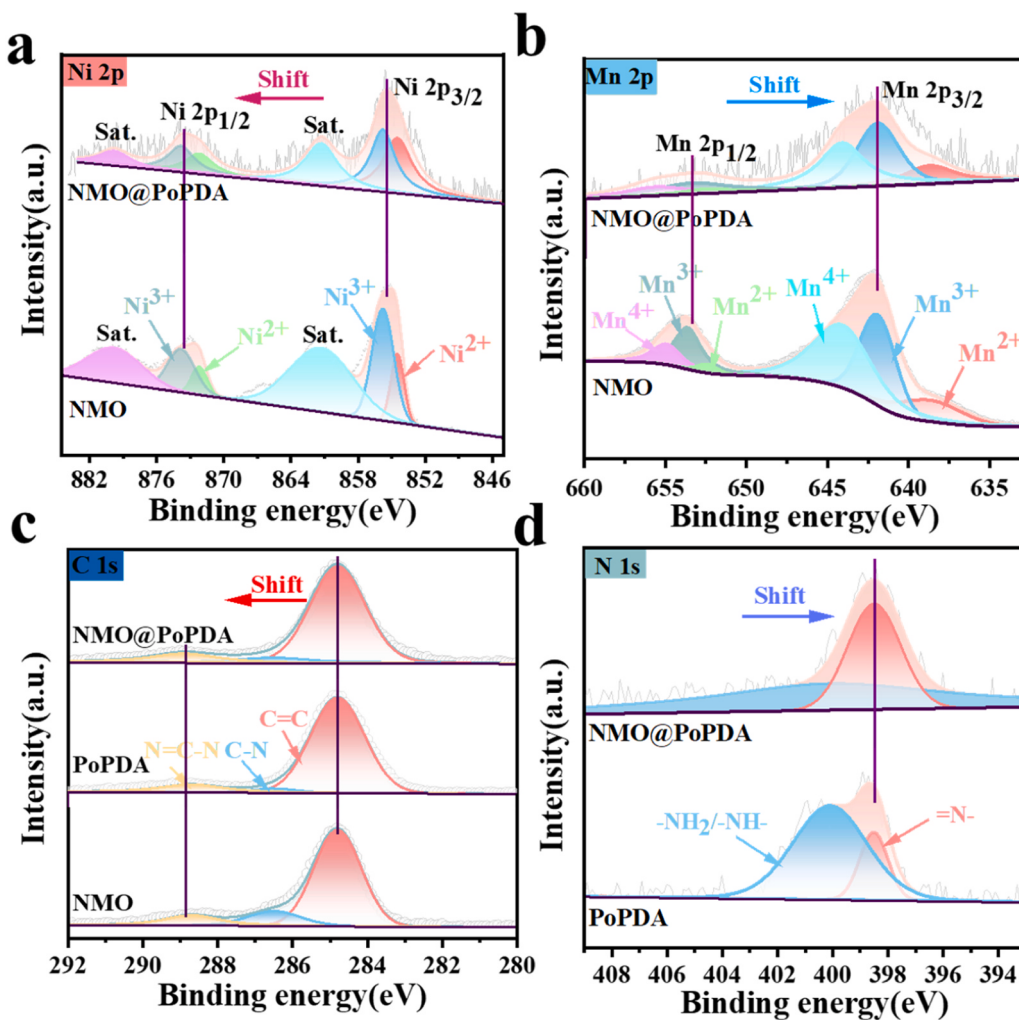
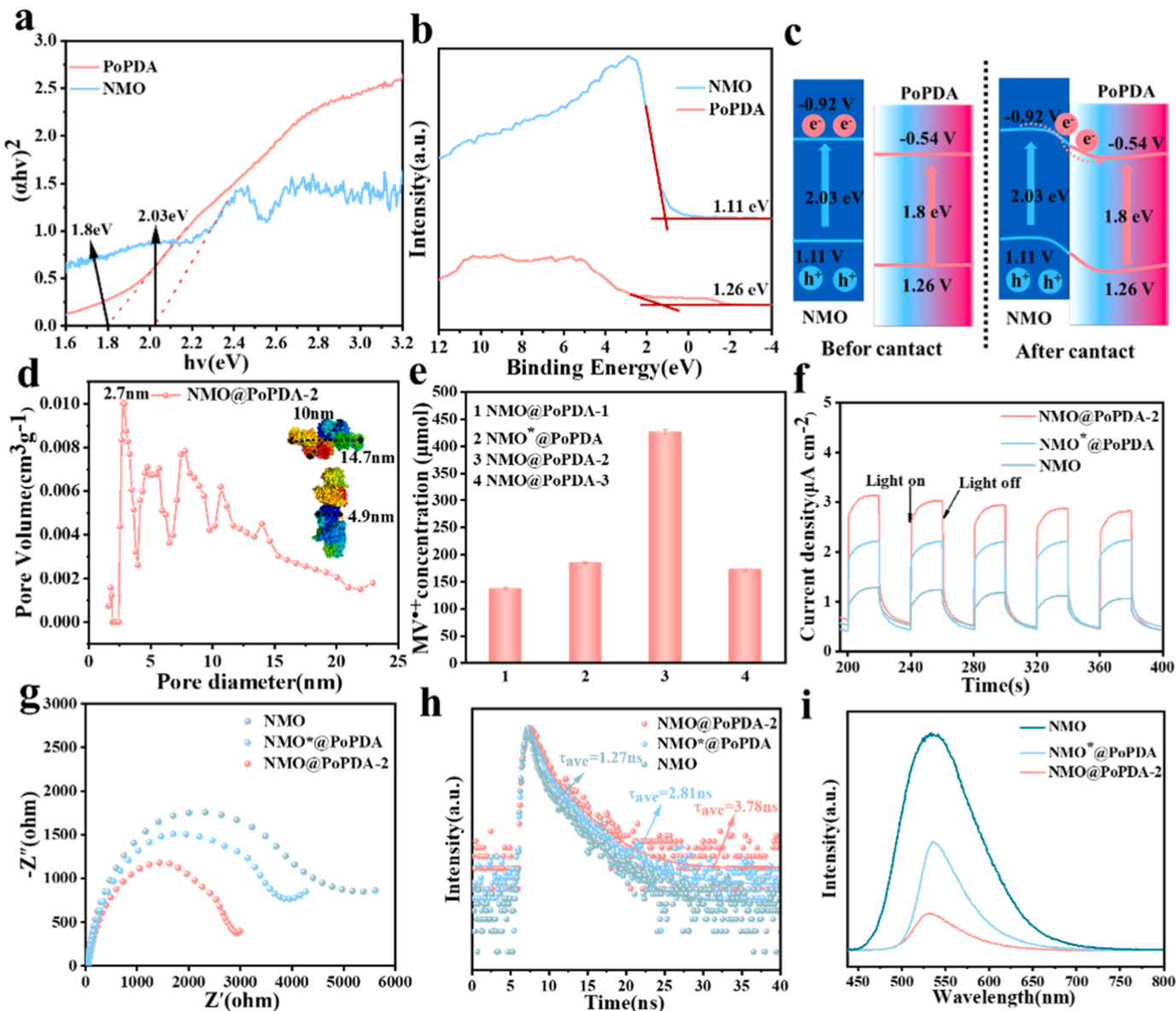


Fig. 3. High-resolution XPS spectra of (a) Ni 2p, (b) Mn 2p, (c) N 1s and (d) C 1s of PoPDA and NMO@PoPDA-2.

photocatalytic activity of NMO and NMO\* samples were also investigated under visible light ( $\lambda \geq 400$  nm) and full-spectrum light irradiation ( $\lambda \geq 300$  nm) (Fig. S9). Under visible light irradiation, no  $MV^{2+}$  production was detected in either pure NMO or pure NMO\*, which could be related to the low separation efficiency of charge carriers (discussed in detail below). However, the NMO ( $13.85 \text{ mmol h}^{-1}\text{g}^{-1}$ ) displays better photocatalytic activity than NMO\* ( $10.77 \text{ mmol h}^{-1}\text{g}^{-1}$ ) under full spectrum irradiation. This result suggests that the fine design and construction of hollow structured materials are advantageous for improving photocatalytic performance [42].

According to the above analysis, the high photocatalytic performance of NMO@PoPDA-2 can be attributed to the following three reasons: Firstly, the hierarchical hollow nanospheres structure benefits to reduce diffusion length and improve electron conductivity for separation and transport of charge carriers; Secondly, the highly conductive artificial thylakoid membrane PoPDA, which increases light absorption capacity and electron transport capacity efficiently; Finally, the PoPDA membrane has excellent absorption capacity for  $MV^{2+}$ . To elucidate the reasons for the high photocatalytic performance of hierarchical hollow NMO@PoPDA-2 nanospheres, a series of photoelectrochemical characterizations were carried out. As shown in Fig. 4f, the transient photocurrent spectrum shows that NMO@PoPDA-2 owns the highest photocurrent density under visible light, perfectly illustrating the hollow structure and encapsulation of PoPDA promoting the separation and transfer of photogenerated charge carriers. Meanwhile, electrochemical impedance spectroscopy (EIS) was used to study the resistance during

interfacial charge transfer (Fig. 4g). Clearly, NMO@PoPDA-2 has the smallest arc radius in Nyquist plot, indicating that the hollow structure and strong interaction between NMO and PoPDA further facilitate the charge transfer. Moreover, the steady-state photoluminescence (PL) spectra and time-resolved photoluminescence (TRPL) spectra were performed to study the charge-carrier separation and transfer efficiency in the NMO@PoPDA-2. As shown in Fig. 4h, PL spectrum suggests that NMO@PoPDA-2 exhibits the weakest PL peak compared to other samples responding to the suppressed electron-hole pairs recombination and enhanced electron transfer behavior in NMO@PoPDA-2. TRPL spectra discloses an increase average carrier lifetime from 1.27 ns for pristine NMO to 3.78 ns for NMO@PoPDA-2 (Fig. 4i). The significantly increased charge carrier lifetime confirms that the modification of PoPDA could extend the photoelectron lifetime of NMO@PoPDA-x and then lead to more efficient transfer of photogenerated electrons [43]. Moreover, steady state photovoltage (SPV) technique were employed to characterize the photo-induced carrier transfer process in the NMO@PoPDA-2 catalyst. The SPV spectrum of NMO@PoPDA-2 reveals that photogenerated electrons can migrate to the surface under light irradiation and meaning the higher separation efficiency compared with pure NMO and PoPDA. From the phase spectrum, the phase of NMO@PoPDA-2 is in the second region (phase value near  $180^\circ$ ), indicating that the photogenerated electrons migrate to the irradiated surface (Fig. S10). All above results fully highlight the benefits of the hierarchical hollow structure in the separation and transfer of photogenerated charge carriers. Of note, surplus PoPDA produces the



**Fig. 4.** (a) UV-vis diffuse reflectance spectra of NMO and PoPDA. (b) VB-XPS spectra of NMO and PoPDA. (c) Schematic electron transfer pathway in NMO@PoPDA-2. (d) pore size distribution of NMO@PoPDA-2 determined by an  $N_2$  adsorption-desorption isotherm curve. The inset gives the size of the CbFDH protein displayed by Pymol software. (e) Photocatalytic regeneration of  $MV^+$  by NMO@PoPDA-x and NMO\*@PoPDA. (f) Transient photocurrent spectra of NMO, NMO\*@PoPDA and NMO@PoPDA-2 under visible light and (g) EIS spectra. (h) Steady state PL spectra and (i) TRPL spectra of NMO, NMO\*@PoPDA and NMO@PoPDA-2.

light-shielding effect and the subdued electronic tunneling effect, which in turn has an impact on the photocatalytic performance (Fig. 4e) [38, 44]. In detail, excess PoPDA blocks the light absorption of the NMO hollow spheres, so charge carriers in the composite NMO@PoPDA-3 are difficult to be successfully excited and separated, causing the light-shielding effect. Moreover, based on the following equation [45]:

$$R_{tu} = \frac{h^2 d}{A e^2 \sqrt{2m\lambda}} \exp\left(\frac{4\pi d}{h} \sqrt{2m\lambda}\right) \quad (2)$$

Herein  $R_{tu}$  is the tunneling resistance,  $h$  is the Planck constant,  $d$  is the tunneling distance of the electron,  $A$  is the cross-sectional area of tunnel,  $e$  is the quantum of electricity,  $\lambda$  is the height of barrier and  $m$  is the mass of electron. It is obvious that the  $R_{tu}$  value becomes larger with the increase of tunneling distance (PoPDA thickness on the NMO surface). Therefore, thicker PoPDA coating causes higher  $R_{tu}$  value and inhibits the transfer of photogenerated electrons from NMO to the PoPDA surface, leading to reduced photocatalytic activity. The adsorption energies

of NMO and NMO@PoPDA for  $MV^{2+}$  are worth studying by DFT calculations. The calculated results show that the adsorption energy of  $MV^{2+}$  on NMO@PoPDA and pristine NMO are  $-0.25$  and  $-0.13$  eV, respectively (Fig. 5a and S11). This result implies that the construction of artificial thylakoid membrane enhanced the adsorption capacity of  $MV^{2+}$ , which in turn affected the photocatalytic activity. In addition to exhibiting superior  $MV^+$  regeneration activity, NMO@PoPDA-2 could be recycled by suction filtration. After 5 cycles, NMO@PoPDA-2 retained 59.7% of the initial activity (Fig. S12). We compared the morphological and structural changes of NMO@PoPDA-2 samples before and after the photocatalytic reaction using XRD, SEM, TEM and XPS (Fig. S13-15).

### 2.3. Photo-enzyme coupled system for the conversion of $CO_2$ to formic

The hierarchical hollow NMO@PoPDA-2 nanospheres with artificial thylakoid membrane were coupled with CbFDH to convert  $CO_2$  to formic

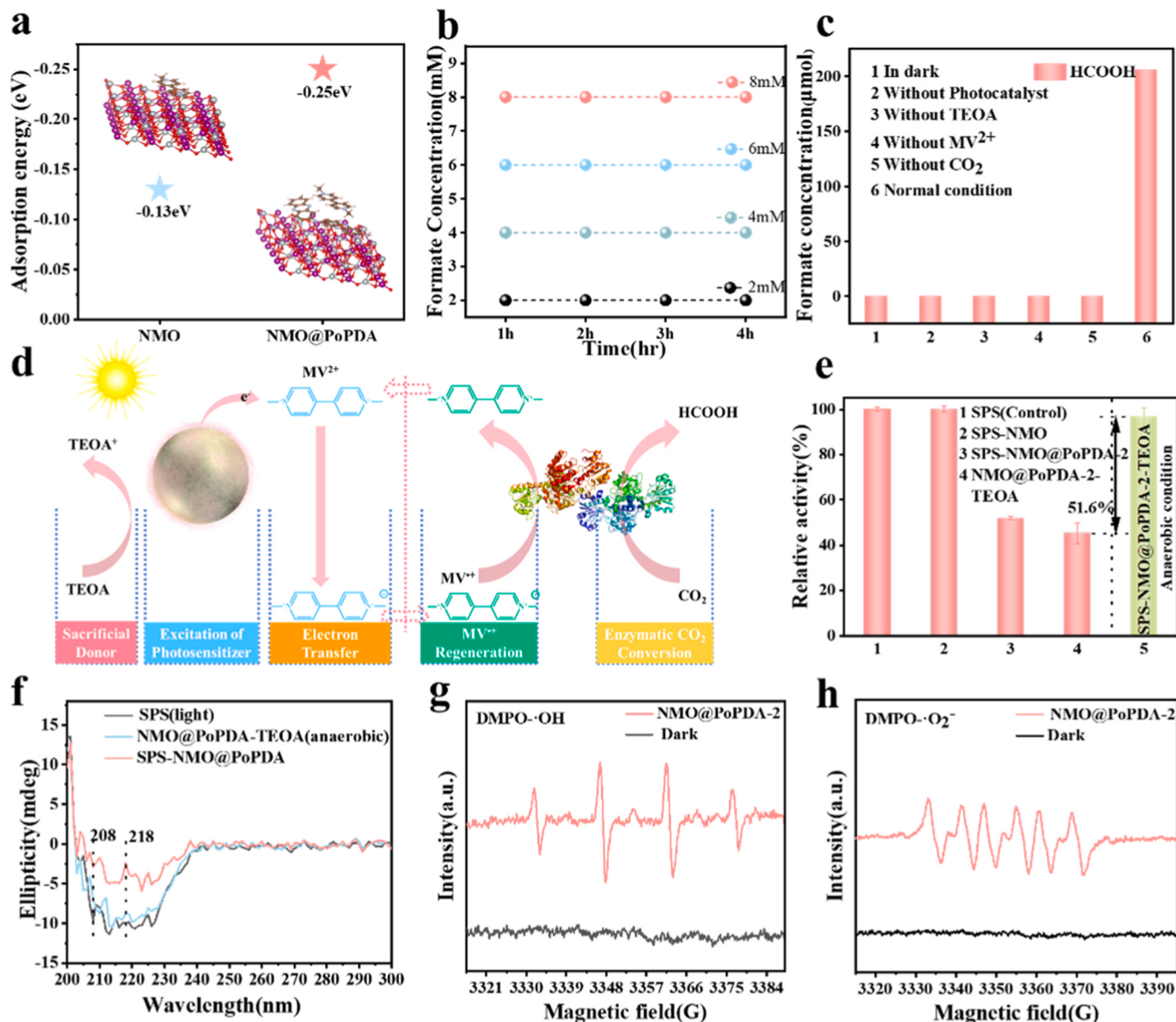


**Fig. 5.** (a) Calculated adsorption energy of MV<sup>2+</sup> on NMO@PoPDA and pristine NMO. (b) Effect of 2 mM MV<sup>2+</sup> on the concentration of sodium formate (2–8 mM) in the presence of 1 unit CbFDH. (c) Concentration of formic acid produced in control experiments under different conditions. (d) Step-by-step diagram of formic acid production from CO<sub>2</sub> reduction by photo-enzyme coupled system. (e) Relative activity. (f) Circular dichroism (CD) spectra of CbFDH after incubation in SPS buffer containing NMO@PoPDA under different conditions. (g) EPR spectra of NMO@PoPDA in aqueous solution (·OH) and (h) methanol solution (O<sub>2</sub><sup>·-</sup>). Reaction condition: (e) [PoPDA or NMO or NMO@PoPDA-2] = 1 mg, CbFDH = 0.1 mg ml<sup>-1</sup>, 0.135 μM NAD<sup>+</sup>, 10 mM formic acid, TEOA = 0 or 400 mM, (anaerobic) SPS buffer (100 mM, pH 7.0), 25 °C.

acid, using MV<sup>2+</sup> as an artificial cofactor. First, we conducted experiments to verify this particular property of MV<sup>2+</sup>, which does not lead to a reverse reaction. MV<sup>2+</sup> and CbFDH reacted with different concentrations of formic acid, and the changes in formic acid and MV<sup>2+</sup> concentrations were analyzed. No changes in formic acid and MV<sup>2+</sup> concentrations were detected even after 6 h, and no significant solution color changes were observed (MV<sup>2+</sup> turned the solution blue) (Fig. 5b and S16). Therefore, it was demonstrated that MV<sup>2+</sup> does not act as a cofactor for the oxidation of formic acid to CO<sub>2</sub> and ensures the accumulation of formic acid produced by CO<sub>2</sub> reduction without loss. In order to avoid side reactions and make CbFDH the best activity, we used sodium pyrophosphate buffer (0.1 M, abbreviated SPS) at pH value of 6.6. In the reduction experiments, CO<sub>2</sub> was present almost exclusively in the form of bicarbonate anion. Thus, we have used bicarbonate (0.1 M) to achieve a high concentration of CO<sub>2</sub> (Eq. 3).



The photobiocatalytic conversion of CO<sub>2</sub> was carried out at 25 °C and anaerobic under visible light illumination ( $\lambda \geq 400$  nm, 300 W) for 2 h. The concentration of formic acid was determined by ion chromatography (DIONEX, ICS-5000). As expected, control experiments (Fig. 5c) showed that no products were detected in the dark or in the absence of carbon source, light, TEOA, MV<sup>2+</sup> and catalyst. The hierarchical hollow NMO@PoPDA-2 nanospheres with artificial thylakoid membrane – CbFDH coupled system could generate 206 μmol formate when TEOA was used as the electron donor. It is evident that the photo-enzyme coupled system for reducing CO<sub>2</sub> to formic acid under visible light has been successfully established (Fig. 5d).

#### 2.4. Compatibility investigation of artificial thylakoid membrane and inactivation mechanism of formate dehydrogenase

In addition to pursuing high performance in  $MV^{2+}$  regeneration capability of photocatalyst, compatibility between photocatalyst and biocatalyst should be achieved to build high efficiency photobiocoupled artificial photosynthesis systems [28]. Given the complex environmental influences that can denature enzymes in the photo-enzyme coupled catalytic process, the impact of various factors on enzymatic activity was evaluated, including light illumination, photocatalyst,  $MV^{2+}$ , TEOA, and ROS. Since the artificial cofactor  $MV^{2+}$  fails to react in reverse when incubated with CbFDH, we added the natural cofactor  $NAD^+$  for formic acid oxidation. Initially, the toxic effects of NMO@PoPDA-2 and different reagents (including  $MV^{2+}$ , TEOA) on the activity of the biocatalyst were evaluated in darkness. As shown in Fig. S17, CbFDH maintained its initial activity after incubation in 0.1 M SPS buffer (pH 7.0) for 1 h, proving that the photocatalyst and reagents are compatible with CbFDH. Then, we also investigated the effect of light on the CbFDH activity (Fig. S18). After 1 h of visible light irradiation, the relative activity of CbFDH was retained at  $74.12 \pm 0.65\%$ . When CbFDH is exposed to light, its subordinate bonds (such as hydrogen bonds) are disrupted, which damages natural conformation of CbFDH, potentially causing loss of biological activity. In the photo-enzyme coupled system, the photogenerated holes could easily deactivate enzymes [28,41], so it is essential to develop biocompatible photocatalysts. Here, since the average pore diameter of the PoPDA membrane was smaller than the size of CbFDH, direct contact between holes and CbFDH can be restricted (Fig. 4d and S19). Obviously, this compartment-like design elevates the compatibility between photocatalyst and CbFDH.

To demonstrate the compatibility of PoPDA artificial thylakoid membrane with CbFDH, the enzyme was incubated under the same conditions without the photocatalyst as the control. The same amount of enzyme ( $0.1 \text{ mg ml}^{-1}$ ) was added to the SPS buffer containing PoPDA-400 mM TEOA and PoPDA, respectively. As shown in Fig. S20, under light illumination at 400 nm for 1 h, the enzyme activity in PoPDA-TEOA decreased slightly to  $96.42 \pm 3.84\%$ , which was much higher than that of PoPDA ( $85.26 \pm 2.63\%$ ). The low activity of the enzyme in buffer without TEOA can be explained as follows: Photogenerated charge carriers and their derived high concentrations of ROS disrupted the  $\alpha$ -helix of the native CbFDH secondary structure and reduced enzymatic activity [28,41]. To verify the above speculation, the activity of CbFDH was investigated in anaerobic SPS buffer. After the removed of  $O_2$ , the activity of CbFDH incubated with PoPDA membrane increased from  $85.26 \pm 2.63\%$  to  $93.62 \pm 1.57\%$  (Fig. S20). These results prove that PoPDA artificial thylakoid membrane has good biocompatibility and bioaffinity, which can effectively compartmentalize photocatalysis and biocatalysis.

In the photo-enzyme coupled catalytic system, to further examine the inactivation mechanism of enzyme, CbFDH was incubated with pure NMO and NMO@PoPDA separately in SPS buffer (containing 0 or 400 mM TEOA). Enzyme activity under visible light irradiation was used as the control. When CbFDH was mixed directly with NMO, its activity remained essentially unchanged after 1 h of illumination (Fig. 5e). According to optical and photoelectrochemical characterization (Fig. 4f-i), the NMO photocatalyst has low charge carrier separation efficiency and high electron-hole recombination rate properties under visible light excitation. As a comparison, the activity of enzyme was  $52.35 \pm 0.35\%$  with NMO@PoPDA photocatalyst co-incubation. Further, TEOA was added and dissolved oxygen was removed from the incubation solution, respectively. After addition of TEOA, the activity of CbFDH incubated with NMO@PoPDA decreased from  $52.35 \pm 0.35\%$  to  $45.22 \pm 4.60\%$ . The decrease in enzyme activity may be related to the fact that the electron donor acts as current-doubling agents facilitating the charge transfer process and accelerating the effective reduction of residual electrons [46], leading to an increase in the concentration of superoxide

radicals ( $O_2^{\bullet-}$ ). Herein, the size-selective PoPDA artificial thylakoid membrane effectively restricted photogenerated holes and enzymes in the inside and outside of PoPDA, respectively. Therefore, the lost activity should be attributed to the  $O_2^{\bullet-}$  from  $O_2$ . The effect of  $O_2^{\bullet-}$  was further investigated by incubating CbFDH and NMO@PoPDA in anaerobic SPS buffer containing 400 mM TEOA. After illumination for 1 h, enzyme activity still retained  $96.80 \pm 3.83\%$ . The circular dichroism (CD) spectrometry was applied to analyze the structure of CbFDH after incubating it with the catalyst under different conditions (Fig. 5f). The CD spectra for CbFDH showed the characteristic bands of an  $\alpha$ -helical structure at 208 and 218 nm, consistent with the  $\pi - \pi^*$  and  $n - \pi^*$  amide transitions of the polypeptide chain, respectively [47]. After incubation with NMO@PoPDA catalysts, the two negative bands at 208 and 218 nm were significantly changed. It has been proven that neighboring  $\alpha$ -helical structures with antiparallel arrangements has a positive impact on the stability of proteins. These differences in the secondary structural fractions suggest that holes and ROS disrupted the skeleton structure of CbFDH and caused the protein unfolding, ultimately leading to variation in enzymatic activity. For enzymes incubated with catalysts under anaerobic conditions, the shapes of the two energy bands remain essentially unchanged.

The presence of ROS species was explored by employing electron paramagnetic resonance (EPR) spectroscopy. Common ROS species such as superoxide and hydroxyl radicals were detected using 5,5-dimethyl-1-pyrroline-N-oxide (DMPO) as trapping agents (Fig. 5g, h). Here, trapping agents are small enough to penetrate the core of NMO@PoPDA nanospheres and investigate the generation of ROS. It is noteworthy that except for  $O_2^{\bullet-}$ , considerable amounts of mainly  $\bullet OH$  could be detected in illuminated samples [48]. These  $\bullet OH$  may originate from water oxidation, from the reaction of  $O_2^{\bullet-}$  (from  $O_2$  reduction) or from other steps in the complex redox chemistry of ROS [49]. Given the rather short half-life of about  $10^{-9} \text{ s}$  in aqueous media, [48] hydroxyl radicals ( $\bullet OH$ ) generated by photocatalyst mainly undergo annihilation before contacting CbFDH. Moreover, considering the much larger volume of enzyme and the protection of artificial thylakoid membrane, the probability of CbFDH inactivation is much smaller. Combined with the above analysis, the deactivation mechanism of the enzyme during the production of formate in the photo-enzyme coupled catalytic system is shown in Fig. 6 (Amino acid residues on the  $\alpha$ -helix of the CbFDH secondary structure are shown in Pymol). In short, the construction of the artificial thylakoid membrane makes the photo-enzyme coupled catalysis system successfully integrate the selectivity of biocatalytic and the unique reactivity of photocatalytic for solar-driven chemical transformation.

### 3. Conclusions

In summary, we explored and constructed a hierarchical hollow structure photocatalyst with artificial thylakoid membrane, and employed  $MV^{2+}$  as an artificial cofactor to couple with enzyme catalysis for fabricating the artificial photosynthesis system. Hierarchical hollow NMO@PoPDA nanospheres were successfully prepared by solvothermal and photoinitiated polymerization method. The strong electronic coupling and favorable band structure between NMO and PoPDA effectively separated the holes and electrons. The system achieved a  $MV^{2+}$  regeneration rate of  $213.59 \pm 4.91 \text{ mmol h}^{-1} \text{ g}^{-1}$  and a formic acid yield of  $206 \mu\text{mol}$ . In the precise  $CO_2$  fixation process, the artificial thylakoid membrane has efficient electron transfer and exceptional light absorption properties to coordinate photocatalytic and biocatalytic reactions. The design of artificial thylakoid membrane with performance as an enzyme protective shield will also open up a new idea for the integration of photo-enzyme coupled system.

### CRediT authorship contribution statement

Jugong Shi: Investigation, Data curation, Methodology, Software,

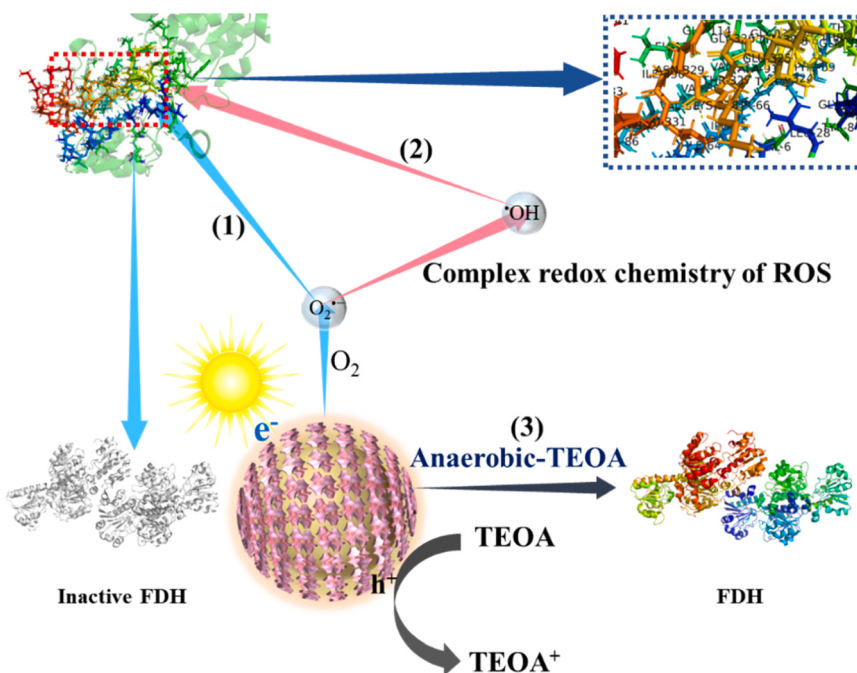


**Fig. 6.** Mechanism of CbFDH inactivation (Demonstration of specific amino acid residues on an  $\alpha$ -helix of CbFDH and hydrogen bonds within 3 Å in Pymol visualization software).

Visualization, Writing – original draft, Visualization. **Shiying Fan:** Methodology, Software, Visualization, Review & editing, Writing – review & editing. **Xinyong Li:** Conceptualization, Formal analysis, Resources, Funds, Writing – review & editing, Supervision. **Penglei Wang:** Methodology, Software, Visualization, Review & editing. **Yan Mao:** Methodology, Software, Visualization, Review & editing. **Mufan Wang:** Methodology, Software, Visualization, Review & editing. **Guohua Chen:** Conceptualization, Writing, Review & editing.

#### Declaration of Competing Interest

The authors declare that they have no known competing financial interests or personal relationships that could have appeared to influence the work reported in this paper.

#### Data availability

Data will be made available on request.

#### Acknowledgements

This work was supported financially by the National Natural Science Foundation of China (Nos. 22076018), the “Xing Liao Talents Program” Project (XLYC1902051), the Program of Introducing Talents of Discipline to Universities (B13012), the Fundamental Research Funds for the Central Universities (DUT19LAB10), the Key Laboratory of Industrial Ecology and Environmental Engineering, China Ministry of Education, and the State Key Laboratory of Catalysis in DICP (N-20-06). Additionally, the authors acknowledge the assistance of DUT Instrumental Analysis Center.

#### Appendix A. Supporting information

Supplementary data associated with this article can be found in the online version at [doi:10.1016/j.apcatb.2023.123434](https://doi.org/10.1016/j.apcatb.2023.123434).

#### References

- [1] F. Hollmann, D.J. Opperman, C.E. Paul, Biocatalytic reduction reactions from a chemist's perspective, *Angew. Chem. -Int. Ed.* 60 (2021) 5644–5665.
- [2] U.T. Bornscheuer, G.W. Huisman, R.J. Kazlauskas, S. Lutz, J.C. Moore, K. Robins, Engineering the third wave of biocatalysis, *Nature* 485 (2012) 185–194.
- [3] A.M. Appel, J.E. Bercaw, A.B. Bocarsly, H. Dobbek, D.L. DuBois, M. Dupuis, J. G. Ferry, E. Fujita, R. Hille, P.J.A. Kenis, C.A. Kerfeld, R.H. Morris, C.H.F. Peden, A. R. Portis, S.W. Ragsdale, T.B. Rauchfuss, J.N. Reek, L.C. Seefeld, R.K. Thauer, G. L. Waldrop, Frontiers, opportunities, and challenges in biochemical and chemical catalysis of  $\text{CO}_2$  fixation, *Chem. Rev.* 113 (2013) 6621–6658.
- [4] E. Lam, M. Miller, S. Linley, R.R. Manuel, I.A.C. Pereira, E. Reisner, Simultaneous conversion of  $\text{CO}_2$  and cellulose to formate using a floating  $\text{TiO}_2$ -Enzyme photoreforming catalyst, *Angew. Chem. (Int. Ed. Engl.)* (2023), e202215894.
- [5] R. Caspi, T. Altman, K. Dreher, C.A. Fulcher, P. Subhraveti, I.M. Keseler, A. Kothari, M. Krummenacker, M. Latendresse, L.A. Mueller, Q. Ong, S. Paley, A. Pujar, A. G. Shearer, M. Travers, D. Weerasinghe, P.F. Zhang, P.D. Karp, The MetaCyc database of metabolic pathways and enzymes and the BioCyc collection of pathway/genome databases, *Nucleic Acids Res.* 40 (2012) D742–D753.
- [6] L. Calzadiaz-Ramirez, A.S. Meyer, Formate dehydrogenases for  $\text{CO}_2$  utilization, *Curr. Opin. Biotechnol.* 73 (2022) 95–100.
- [7] G. Lin, Y.Y. Zhang, Y.T. Hua, C.H. Zhang, C.C. Jia, D.X. Ju, C.M. Yu, P. Li, J. Liu, Bioinspired metalation of the metal-organic framework MIL-125-NH<sub>2</sub> for photocatalytic NADH regeneration and gas-liquid-solid three-phase enzymatic  $\text{CO}_2$  reduction, *Angew. Chem. -Int. Ed.* 61 (2022).
- [8] X.D. Wang, T. Saba, H.H.P. Yiu, R.F. Howe, J.A. Anderson, J.F. Shi, Cofactor NAD (P)H regeneration inspired by heterogeneous pathways, *Chem* 2 (2017) 621–654.
- [9] S.K. Kuk, R.K. Singh, D.H. Nam, R. Singh, J.K. Lee, C.B. Park, Photoelectrochemical reduction of carbon dioxide to methanol through a highly efficient enzyme cascade, *Angew. Chem. -Int. Ed.* 56 (2017) 3827–3832.
- [10] G. Wang, C.T. He, R. Huang, J.J. Mao, D.S. Wang, Y.D. Li, Photoinduction of Cu single atoms decorated on  $\text{UiO}-66-\text{NH}_2$  for enhanced photocatalytic reduction of  $\text{CO}_2$  to liquid fuels, *J. Am. Chem. Soc.* 142 (2020) 19339–19345.
- [11] F. Sastre, A.V. Puga, L.C. Liu, A. Corma, H. Garcia, Complete photocatalytic reduction of  $\text{CO}_2$  to methane by h2 under solar light irradiation, *J. Am. Chem. Soc.* 136 (2014) 6798–6801.
- [12] K. Kamada, J. Jung, T. Wakabayashi, K. Sekizawa, S. Sato, T. Morikawa, S. Fukuzumi, S. Saito, Photocatalytic  $\text{CO}_2$  reduction using a Robust multifunctional iridium complex toward the selective formation of formic acid, *J. Am. Chem. Soc.* 142 (2020) 10261–10266.
- [13] K. Li, B.S. Peng, T.Y. Peng, Recent advances in heterogeneous photocatalytic  $\text{CO}_2$  conversion to solar fuels, *Acc. Catal.* 6 (2016) 7485–7527.
- [14] Z.R. Miao, Q.L. Wang, Y.F. Zhang, L.P. Meng, X.X. Wang, In situ construction of S-scheme  $\text{AgBr}/\text{BiOBr}$  heterojunction with surface oxygen vacancy for boosting photocatalytic  $\text{CO}_2$  reduction with  $\text{H}_2\text{O}$ , *Appl. Catal. B-Environ.* 301 (2022).
- [15] W.B. Liu, X.K. Li, C.M. Wang, H.H. Pan, W.P. Liu, K. Wang, Q.D. Zeng, R.M. Wang, J.Z. Jiang, A scalable general synthetic approach toward ultrathin imine-linked two-dimensional covalent organic framework nanosheets for photocatalytic  $\text{CO}_2$  reduction, *J. Am. Chem. Soc.* 141 (2019) 17431–17440.

[16] W.F. Zhong, R.J. Sa, L.Y. Li, Y.J. He, L.Y. Li, J.H. Bi, Z.Y. Zhuang, Y. Yu, Z.G. Zou, A covalent organic framework bearing single Ni sites as a synergistic photocatalyst for selective photoreduction of CO<sub>2</sub> to CO, *J. Am. Chem. Soc.* 141 (2019) 7615–7621.

[17] R.K. Yadav, A. Kumar, N.J. Park, D. Yadav, J.O. Baeg, New carbon nanodots-silica hybrid photocatalyst for highly selective solar fuel production from CO<sub>2</sub>, *Chemcatchem* 9 (2017) 3153–3159.

[18] P.M. Stanley, C. Thomas, E. Thyrhaug, A. Urstoege, M. Schuster, J. Hauer, B. Rieger, J. Warman, R.A. Fischer, Entrapped molecular photocatalyst and photosensitizer in metal- organic framework nanoreactors for enhanced solar CO<sub>2</sub> reduction, *Acs Catal.* 11 (2021) 871–882.

[19] N.Y. Huang, H. He, S.J. Liu, H.L. Zhu, Y.J. Li, J. Xu, J.R. Huang, X. Wang, P.Q. Liao, X.M. Chen, Electrostatic attraction-driven assembly of a metal-organic framework with a photosensitizer boosts photocatalytic CO<sub>2</sub> reduction to CO, *J. Am. Chem. Soc.* 143 (2021) 17424–17430.

[20] F. Arcudi, L. Dordevic, B. Nagasing, S.I. Stupp, E.A. Weiss, Quantum dot-sensitized photoreduction of CO<sub>2</sub> in water with turnover number > 80,000, *J. Am. Chem. Soc.* 143 (2021) 18131–18138.

[21] K.M. Cho, K.H. Kim, K. Park, C. Kim, S. Kim, A. Al-Saggaf, I. Gereige, H.T. Jung, Amine-functionalized graphene/CdS composite for photocatalytic reduction of CO<sub>2</sub>, *Acs Catal.* 7 (2017) 7064–7069.

[22] B.S. Jayathilake, S. Bhattacharya, N. Vaidehi, S.R. Narayanan, Efficient and selective electrochemically driven enzyme-catalyzed reduction of carbon dioxide to formate using formate dehydrogenase and an artificial cofactor, *Acc. Chem. Res.* 52 (2019) 676–685.

[23] R. Barin, D. Biria, S. Rashid-Nadimi, M.A. Asadollahi, Enzymatic CO<sub>2</sub> reduction to formate by formate dehydrogenase from *Candida boidinii* coupling with direct electrochemical regeneration of NADH, *J. CO<sub>2</sub> Util.* 28 (2018) 117–125.

[24] M.A. Jensen, P.J. Elving, Nicotinamide adenine-dinucleotide (NAD<sup>+</sup>) - formal potential of the NAD<sup>+</sup> NAD. Couple and nad. dimerization rate, *Biochim. Et. Biophys. Acta* 764 (1984) 310–315.

[25] S. Ikeyama, Y. Amao, A novel electron carrier molecule based on a viologen derivative for visible light-driven CO<sub>2</sub> reduction to formic acid with the system of zinc porphyrin and formate dehydrogenase, *Sustainable, Energy Fuels* 1 (2017) 1730–1733.

[26] S. Ikeyama, Y. Amao, An artificial Co-enzyme based on the viologen skeleton for highly efficient CO<sub>2</sub> reduction to formic acid with formate dehydrogenase, *Chemcatchem* 9 (2017) 833–838.

[27] S.B. Wang, B.Y. Guan, L. Yu, X.W. Lou, Rational Design of Three-Layered TiO<sub>2</sub>@Carbon@MoS<sub>2</sub> Hierarchical Nanotubes for Enhanced Lithium Storage, *Adv. Mater.* 29 (2017).

[28] S.H. Zhang, S.S. Liu, Y.Y. Sun, S.A. Li, J.F. Shi, Z.Y. Jiang, Enzyme-photo-coupled catalytic systems, *Chem. Soc. Rev.* 50 (2021) 13449–13466.

[29] Z.W. Tong, D. Yang, Z. Li, Y.H. Nan, F. Ding, Y.C. Shen, Z.Y. Jiang, Thylakoid-inspired multishell g-C<sub>3</sub>N<sub>4</sub> nanocapsules with enhanced visible-light harvesting and electron transfer properties for high-efficiency photocatalysis, *Acs Nano* 11 (2017) 1103–1112.

[30] T. Mirkovic, E.E. Ostroumov, J.M. Anna, R. van Grondelle, G.D. Govindjee, Scholes, Light absorption and energy transfer in the antenna complexes of photosynthetic organisms, *Chem. Rev.* 117 (2017) 249–293.

[31] L.L. Sun, C.Y. Liu, J.Z. Li, Y.J. Zhou, H.Q. Wang, P.W. Huo, C.C. Ma, Y.S. Yan, Fast electron transfer and enhanced visible light photocatalytic activity by using poly-o-phenylenediamine modified AgCl/g-C<sub>3</sub>N<sub>4</sub> nanosheets, *Chin. J. Catal.* 40 (2019) 80–94.

[32] S. Liu, J.Q. Tian, L. Wang, Y.W. Zhang, X.Y. Qin, Y.L. Luo, A.M. Asiri, A.O. Al-Youbi, X.P. Sun, Hydrothermal treatment of grass: a low-cost, green route to nitrogen-doped, carbon-rich, photoluminescent polymer nanodots as an effective fluorescent sensing platform for label-free detection of Cu(II) ions, *Adv. Mater.* 24 (2012) 2037–2041.

[33] M.C. Qin, S.Y. Fan, X.Y. Li, Z.D. Niu, C.P. Bai, G.H. Chen, Highly efficient electrocatalytic upgrade of n-valeraldehyde to octane over Au SACs-NiMn<sub>2</sub>O<sub>4</sub> spinel synergistic composites, *Small* 18 (2022).

[34] X. Zhang, G.F. Li, J.X. Wang, J. Chu, F. Wang, Z.J. Hu, Z.P. Song, Revisiting the structure and electrochemical performance of Poly(o-phenylenediamine) as an organic cathode material, *Acs Appl. Mater. Interfaces* 14 (2022) 27968–27978.

[35] M. Zhang, S.H. Guo, L. Zheng, G.N. Zhang, Z.P. Hao, L.P. Kang, Z.H. Liu, Preparation of NiMn<sub>2</sub>O<sub>4</sub> with large specific surface area from an epoxide-driven sol-gel process and its capacitance, *Electrochim. Acta* 87 (2013) 546–553.

[36] S.B. Wang, B.Y. Guan, X.W. Lou, Rationally designed hierarchical N-doped carbon@NiCo<sub>2</sub>O<sub>4</sub> double-shelled nanoboxes for enhanced visible light CO<sub>2</sub> reduction, *Energy Environ. Sci.* 11 (2018) 306–310.

[37] M.C. Qin, S.Y. Fan, X.Y. Li, M.O. Tade, S.M. Liu, Electroreductive C-O coupling of benzaldehyde over SACs Au-NiMn<sub>2</sub>O<sub>4</sub> spinel synergistic composites, *J. Colloid Interface Sci.* 625 (2022) 305–316.

[38] A.Y. Meng, B. Cheng, H.Y. Tan, J.Y. Fan, C.L. Su, J.G. Yu, TiO<sub>2</sub>/polydopamine S-scheme heterojunction photocatalyst with enhanced CO<sub>2</sub>-reduction selectivity, *Appl. Catal. B-Environ.* 289 (2021).

[39] Y. Jiang, H.Y. Chen, J.Y. Li, J.F. Liao, H.H. Zhang, X.D. Wang, D.B. Kuang, Z-scheme 2D/2D heterojunction of CsPbBr<sub>3</sub>/Bi<sub>2</sub>WO<sub>6</sub> for improved photocatalytic CO<sub>2</sub> reduction, *Adv. Funct. Mater.* 30 (2020).

[40] B.A. Parkinson, P.F. Weaver, Photoelectrochemical pumping of enzymatic CO<sub>2</sub> reduction, *Nature* 309 (1984) 148–149.

[41] Y.Y. Sun, J.F. Shi, Z. Wang, H. Wang, S.H. Zhang, Y.Z. Wu, H.J. Wang, S.H. Li, Z. Y. Jiang, Thylakoid membrane-inspired capsules with fortified cofactor shuttling for enzyme-photocoupled catalysis, *J. Am. Chem. Soc.* 144 (2022) 4168–4177.

[42] S.B. Wang, B.Y. Guan, X. Wang, X.W. Lou, Formation of hierarchical Co<sub>9</sub>S<sub>8</sub>@ZnIn<sub>2</sub>S<sub>4</sub> heterostructured cages as an efficient photocatalyst for hydrogen evolution, *J. Am. Chem. Soc.* 140 (2018) 15145–15148.

[43] S. Gao, B.C. Gu, X.C. Jiao, Y.F. Sun, X.L. Zu, F. Yang, W.G. Zhu, C.M. Wang, Z. M. Feng, B.J. Ye, Y. Xie, Highly efficient and exceptionally durable CO<sub>2</sub> photoreduction to methanol over freestanding defective single-unit-cell bismuth vanadate layers, *J. Am. Chem. Soc.* 139 (2017) 3438–3445.

[44] N. Hu, Y. Karube, C. Yan, Z. Masuda, H. Fukunaga, Tunneling effect in a polymer/carbon nanotube nanocomposite strain sensor, *Acta Mater.* 56 (2008) 2929–2936.

[45] P.F. Xia, M.J. Liu, B. Cheng, J.G. Yu, L.Y. Zhang, Dopamine modified g-C<sub>3</sub>N<sub>4</sub> and its enhanced visible-light photocatalytic H<sub>2</sub>-production activity, *ACS Sustain. Chem. Eng.* 6 (2018) 8945–8953.

[46] F. Costantino, P.V. Kamat, Do sacrificial donors donate H<sub>2</sub> in photocatalysis? *Acs Energy Lett.* 7 (2022) 242–246.

[47] L.Z. Liu, W. Yu, D. Luo, Z.J. Xie, X.Y. Qin, X.H. Sun, J.C. Zhao, J.L. Wang, T. Wang, Catalase nanocapsules protected by polymer shells for scavenging free radicals of tobacco smoke, *Adv. Funct. Mater.* 25 (2015) 5159–5165.

[48] W.Y. Zhang, E. Fernandez-Fueyo, Y. Ni, M. van Schie, J. Gacs, R. Renirie, R. Wever, F.G. Mutti, D. Rother, M. Alcalde, F. Hollmann, Selective aerobic oxidation reactions using a combination of photocatalytic water oxidation and enzymatic oxyfunctionalizations, *Nat. Catal.* 1 (2018) 55–62.

[49] J. Schneider, M. Matsuoka, M. Takeuchi, J.L. Zhang, Y. Horiuchi, M. Anpo, D. W. Bahnemann, Understanding TiO<sub>2</sub> photocatalysis: mechanisms and materials, *Chem. Rev.* 114 (2014) 9919–9986.